Geophysical Research Letters

Supporting Information for

Human Water Use Impacts on the Strength of the Continental Sink for Atmospheric Water

Jessica Keune[1,2,3,†,*], Mauro Sulis[4], Stefan Kollet[1,3], Stefan Siebert[5,6] and Yoshihide Wada[7,8]

[1] Institute for Bio- and Geosciences, Agrosphere (IBG-3), Research Centre Jülich, Jülich, Germany, **[2]** Meteorological Institute, University of Bonn, Bonn, Germany, **[3]** Centre for High-Performance Scientific Computing in Terrestrial Systems, Geoverbund ABC/J, Jülich, Germany, **[4]** Luxembourg Institute of Science and Technology, Environmental Research and Innovation, Belvaux, Luxembourg, **[5]** Institute of Crop Science and Resource Conservation, University of Bonn, Bonn, Germany, **[6]** Department of Crop Sciences, University of Göttingen, Göttingen, Germany, **[7]** International Institute for Applied Systems Analysis, Laxenburg, Austria, **[8]** Department of Physical Geography, Utrecht University, Utrecht, The Netherlands

Corresponding author: Jessica Keune (jkeune@uni-bonn.de)

[†] Now at: Laboratory of Hydrology and Water Management, Ghent University, Ghent, Belgium

Contents of this file

Text S1 to S6
Figures S1 to S14
Table S1

Introduction

This supporting information provides additional information on

1. The Modeling System
2. Land-atmosphere water balance
3. Computational costs
4. Human water use data
5. Results – supporting figures and tables
6. Validation of the simulations with in-situ observations

1 Modeling System

In this study, we used the Terrestrial Systems Modeling Platform (TerrSysMP v1.2.0MCT, Shrestha et al., 2014; Gasper et al., 2014), which consists of the atmospheric model COSMO (Version 5.1, Baldauf et al., 2011; Doms & Schättler, 2002), the Community Land Model CLM (Version 3.5, Oleson et al., 2008) and the variably saturated surface-subsurface flow model ParFlow (Kollet & Maxwell, 2006; Jones & Woodward, 2001) coupled through OASIS-MCT (Valcke, 2013). TerrSysMP has already been set up over the European CORDEX domain at 0.11° (~12.5 km) resolution in previous studies (Keune et al., 2016) and simulates close-to-physics 3D groundwater dynamics and groundwater-surface water interactions, the land surface moisture, energy and momentum balance, and atmospheric transport in a fully-coupled fashion.

In this study, COSMO5.1 was nested into 3-hourly boundary fields from ERA-Interim (Dee et al., 2011; 0.5° resolution). Additional 3, 6 and 9h forecasts from ERA-Interim analysis at 00 and 12 UTC were used to update the lateral boundaries every 3 hours. The following 3D fields and geopotential are downscaled to 0.11° resolution and used for initialization and lateral boundaries: specific humidity, temperature, wind, cloud liquid, and ice water content. In order to keep the large-scale atmosphere consistent between all simulations, we applied the spectral nudging technique (von Storch et al., 2000) for horizontal wind components only (u,v) above the planetary boundary layer (<850 hPa) for wavenumbers smaller than 14 with alpha=0.05. We used the following physical parameterizations to account for subgrid-scale processes: Convection was parameterized using the Tiedtke mass flux scheme (Tiedke, 1989). The δ-two-stream approximation of the radiative transfer equation according to Ritter & Geleyn (1992) was used. Vertical turbulent diffusion was simulated with a 2.5-level closure scheme based on the prognostic equation for turbulent kinetic energy. Cloud microphysics were simulated with a bulk-water continuity model, predicting cloud water, cloud ice, rain, and snow. COSMO's time step was 60 seconds, while CLM and ParFlow were applied with 180 seconds timesteps. Coupling took place every 180 seconds.

The land surface characteristics for CLM3.5 were based on previous studies (Keune et al., 2016) and include land cover from the Moderate Resolution Imaging Spectroradiometer (MODIS, Friedl et al., 2002) data set, accounting for subgrid heterogeneity by employing a maximum of 4 plant functional types per grid cell. In addition, the leaf area index was updated using the MODIS 2000 data set.

ParFlow was set up with the hydrofacies distribution 2 (HFD2) from Keune et al. (2016) in order to represent vertically heterogeneous soil and hydrogeologic characteristics. This HFD consists of the FAO database for the upper ten soil layers (reaching a depth of 3 m) and five bottom soil layers representing the deeper subsurface and bedrock hydrogeology using the Gleeson (Gleeson et al., 2011) database. The vertical discretization increases with depth to reach a total of 103 m subsurface depths. At the coastlines, a lateral Dirichlet boundary condition was applied with a hydrostatic profile, which mimics the ocean with a free water table at the top.

Five simulations were carried out covering the full calendar year 2003. In addition to four human water use simulations, one natural reference simulation (NAT) was performed, which does not consider any human water use. The water use simulations were constructed as follows in order to account for the uncertainty of daily pumping and irrigation estimates applied in the simulations, and the atmospheric feedback by perturbing the water use schedule. Irrigation and (total) groundwater abstraction estimates were taken from Wada et al. (2012), Wada et al. (2016) and Siebert et al. (2010), Siebert and Döll (2010). Total groundwater abstraction (abstraction for irrigation, domestic and industrial demand) was applied, and estimates of domestic and industrial demand from Wada et al. (2012), Wada et al. (2016) were added to groundwater abstraction estimates for irrigation from Siebert et al. (2010) and Siebert an Döll (2010) for consistency. Note that while we did not represent surface water abstraction explicitly, total irrigation includes water from surface water and groundwater in all model simulations. The two data sets with an original resolution of 0.1° were bilinearly interpolated in space to match the CORDEX grid. Two water use schedules, i.e. daytime (06:00–18:00 UTC) and nighttime (18:00 - 06:00 UTC) were generated for each data set, resulting in a total of four water use scenarios. The hourly rates of each daily estimate were added to the top soil layer (irrigation) or subtracted from the bottom soil layer (groundwater abstraction/pumping) in ParFlow via straight-forward source/sink terms in the governing equations. Irrigation and pumping were applied simultaneously in the model. All simulations started from the same quasi-equilibrium initial condition, which was achieved by a multi-year spin-up of the NAT simulation using atmospheric forcing from the year 2003. The first 5 days of each simulation were neglected for analysis.

2 Land-atmosphere water balance

In a natural system, the terrestrial hydrologic cycle extends from the subsurface over the land surface to the atmosphere, connecting the land surface/subsurface water balance

$$(\partial S/\partial t)_{\mathrm{NAT}} = P_{\mathrm{NAT}} - ET_{\mathrm{NAT}} - (\mathrm{div}(Q_g))_{\mathrm{NAT}} - R_{\mathrm{NAT}} \qquad \textbf{(1)}$$

with the atmospheric water balance

$$(\partial W/\partial t)_{\mathrm{NAT}} = -P_{\mathrm{NAT}} + ET_{\mathrm{NAT}} - (\mathrm{div}(Q))_{\mathrm{NAT}} \qquad \textbf{(2)}$$

via precipitation P and evapotranspiration ET.

Terrestrial water storage changes arise through the balance of P, ET, runoff (R) and groundwater divergence $\mathrm{div}(Q_g) = \nabla \cdot Q_g$. Vice versa, the atmospheric moisture storage can only be altered through P, ET and the atmospheric moisture divergence $\mathrm{div}(Q)$. The atmospheric moisture divergence $\mathrm{div}(Q)$ is the vertically integrated horizontal moisture transport defined as

$$div(Q) = -\frac{1}{g}\nabla \cdot \int_0^{p_s} q\vec{V}dp \quad , \qquad \textbf{(3)}$$

with the gravitational acceleration g, specific humidity q, horizontal wind vector $\boldsymbol{V}$, pressure p and surface pressure p_s. As the atmospheric water storage is relatively small and its temporal change is even smaller ($(\partial W/\partial t) \approx 0$) even over relatively short time scales, the atmospheric moisture divergence $\mathrm{div}(Q)$ is mainly driven by P and ET, i.e.

$$\mathrm{div}(Q) = P - ET \qquad \textbf{(4)}$$

We define continental sink C_{SI} and continental source C_{SO} based on the atmospheric divergence, i.e. $C_{SI} = -\mathrm{div}(Q) = P-ET$ for $P>ET$ and $C_{SO} = \mathrm{div}(Q) = ET-P$ for $P<ET$. Furthermore, substitution of equation 1 into equation 4 combines the atmospheric and land surface/subsurface water balances in a natural system

$$(\mathrm{div}(Q))_{\mathrm{NAT}} = -(\partial S/\partial t)_{\mathrm{NAT}} - (\mathrm{div}(Q_g))_{\mathrm{NAT}} - R_{\mathrm{NAT}} \quad \textbf{(5)}$$

and shows that the land surface/subsurface act as a sink/source for atmospheric water. We calculate div(Q) as the residual of equation (2) based on hourly outputs of P and ($\partial W/\partial t$) from COSMO, and ET from CLM, respectively. Figure 2 of the main manuscript illustrates simulated cumulative $(\mathrm{div}(Q))_{\mathrm{NAT}}$, for each grid cell over a year, the summer months (June-July-August), and for August. For the watershed calculation of div(Q), we used the watershed boundaries from HydroSHEDS (Global Hydrological data and maps based on Shuttle Derivatives at multiple Scales, Lehner et al., 2006) at 30 arc seconds (~1km). div(Q) was summarized over the year, summer months and August and the average of all grid cell values within each watershed was calculated.

The natural hydrologic cycle, as described above, is systematically altered through human water use (HWU), here considered as groundwater pumping G and irrigation I. Hence, in a managed system, the natural land surface balance is disturbed

$$(\partial S/\partial t)_{\mathrm{HWU}} = P_{\mathrm{HWU}} - ET_{\mathrm{HWU}} - (\mathrm{div}(Q_g))_{\mathrm{HWU}} - R_{\mathrm{HWU}} \quad \textbf{(6)}$$

and might exhibit systematic differences compared to the natural reference system in evapotranspiration

$$\Delta ET = ET_{\mathrm{HWU}} - ET_{\mathrm{NAT}}, \quad \textbf{(7a)}$$

in precipitation,

$$\Delta P = P_{\mathrm{HWU}} - P_{\mathrm{NAT}}, \quad \textbf{(7b)}$$

and, thus, in atmospheric divergence,

$$\Delta(\mathrm{div}(Q)) = (\mathrm{div}(Q))_{\mathrm{HWU}} - (\mathrm{div}(Q))_{\mathrm{NAT}}, \quad \textbf{(7c)}$$

and subsurface water storage,

$$\Delta(\partial S/\partial t) = (\partial S/\partial t)_{\mathrm{HWU}} - (\partial S/\partial t)_{\mathrm{NAT}}. \quad \textbf{(7d)}$$

The deviations illustrated here account for the integrated, nonlinear feedbacks of the system, i.e. ΔET accounts for the difference in ET induced by $I-G$, but also for the ET feedbacks on P, which in turn affect ET in a nonlinear feedback loop.

div(Q) was calculated for each human water use scenario separately and averaged over all grid cells within each watershed. The difference between the natural and human water use were calculated as described in equations (7a) to (7d).

For the consistency check, div(Q) values were averaged over all terrestrial grid cells in each PRUDENCE (Christensen & Christensen, 2007) region. The PRUDENCE regions have the following extensions (W,E,S,N): Iberian Peninsula, IB (-10,3,36,44); British Isles, BI (-10,2,50,59); Mid-Europe, ME (2,16,48,55); Mediterranean, MD (3,25,26,44); Eastern Europe, EA (16,30,44,55), Alps, AL (5,15,44,48), France, FR (-5,5,44,50); and Scandinavia, SC (5,30,55,70). For the CORDEX domain average, a sponge zone was removed from the domain and the average over all terrestrial grid cells in a focus domain (Fig. 2) was calculated. To evaluate the consistency, the total annual, summer and August differences $\Delta(\mathrm{div}(Q))_{\mathrm{HWU1}}$ were plotted against $\Delta(\mathrm{div}(Q))_{\mathrm{HWU2}}$, averaged over the PRUDENCE regions, the watersheds and single grid points.

As described in equations (6) and (7d), the human water use induced feedbacks contribute to drying or wetting. We calculate the subsurface storage S for each simulation, over all terrestrial grid cells and the full soil column of each cell, containing the fully saturated and the variably saturated zones. For one cell, the storage is the sum of water in each layer k of thickness Δz_k, i.e.

$$S = \sum_{k=1}^{K} [s_k \phi \Delta z_k], \quad \textbf{(8)}$$

with relative saturation s, and porosity ϕ. Because all simulations start with the same initial terrestrial water storage, we can directly compare the total storages of the natural and managed systems at the end of the simulations, i.e.

$$\Delta S = \Delta(\partial S/\partial t) = (\partial S/\partial t)_{\mathrm{HWU}} - (\partial S/\partial t)_{\mathrm{NAT}} = S_{\mathrm{end,HWU}} - S_{\mathrm{end,NAT}} \quad \textbf{(9)}$$

and analyze how human water use induced changes of the continental sink $\Delta(\mathrm{div}(Q))$ translate into water storage changes according to

$$\Delta(\partial S/\partial \mathrm{t}) = \; = \Delta(\mathrm{div}(Q)) - [\Delta(\mathrm{div}(Q_{\mathrm{g}})) + \Delta R] \qquad \mathbf{(10)}$$

A storage change according to equation (9) was calculated for each grid cell and averaged over the grid cells in each watershed. To illustrate the relation of ΔS and $\Delta(\mathrm{div}(Q))$ from equation (10), we calculated annual $\Delta(\mathrm{div}(\mathrm{Q}))$ averaged over each watershed and plotted the values against ΔS. Deviations from the 1:1 line in Fig. 5 of the main manuscript are thus due to changes in lateral surface-subsurface flow, i.e. groundwater divergence and runoff $[\Delta(\mathrm{div}(Q_{\mathrm{g}})) + \Delta R]$ in equation (10). For visualization, no changes (ΔS=0 or $\Delta(\mathrm{div}(Q))$=0) were neglected in Fig. 5 and the slope of the relationship changed because of sign changes for logarithmic scaling.

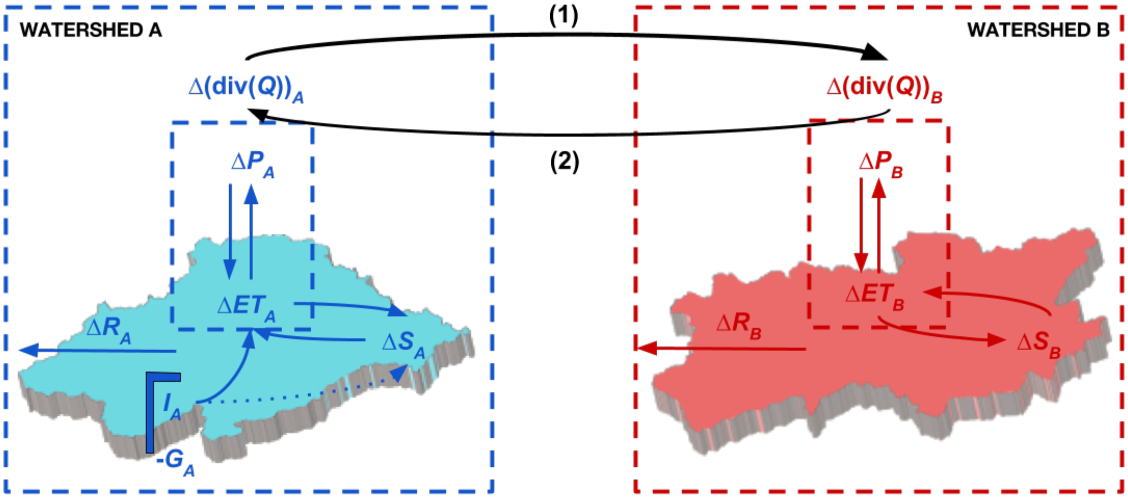

Figure S1. How human water use can alter the continental sink of moisture across watersheds. In a managed watershed A the natural water balance is disturbed through human water use (groundwater pumping G and irrigation I) induced changes of water storage ΔS, runoff ΔR, evapotranspiration ΔET and precipitation ΔP. First, local feedbacks to human water use alter the continental sink of watershed A, and the atmospheric water vapor transport $\mathrm{div}(Q)$ between remote watersheds A and B, which can trigger or inhibit precipitation initiation in watershed B. Secondly, these remotely induced changes of the continental sink and water storage of watershed B can further feedback to watershed A (two-way feedback).

3 Computational costs

All simulations were carried out on the Cray XC40 high-performance computing system at the European Centre for Medium Range Weather Forecasts (ECMWF). Each simulation was run on 14 nodes (with each 36 tasks, i.e. 504 total tasks), split into 12x12 (144) tasks for ParFlow, 6x6 (36) tasks for CLM3.5 and 18x18 (324) tasks for COSMO. One year of simulation required on average about 1.223.067 SBUs (~75.919 core hours).

4 Human water use data

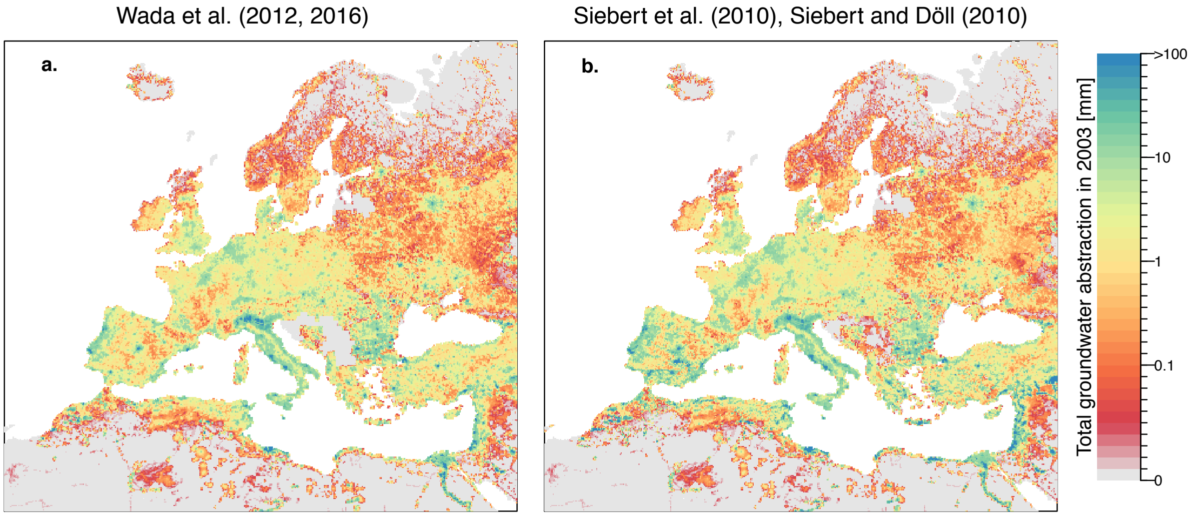
Wada et al. (2012, 2016)

Siebert et al. (2010), Siebert and Döll (2010)

Figure S2. Total groundwater abstraction [mm] from both data sets, (a) HWU1, Wada et al. (2012,2016) and (b) HWU2, Siebert et al. (2010), Siebert and Döll (2010), interpolated to the European CORDEX domain at 0.11° resolution. Note that groundwater abstraction for industrial and domestic use from Wada et al. (2012, 2016) were added to groundwater abstraction from Siebert et al. (2010), Siebert and Döll (2010) for consistency.

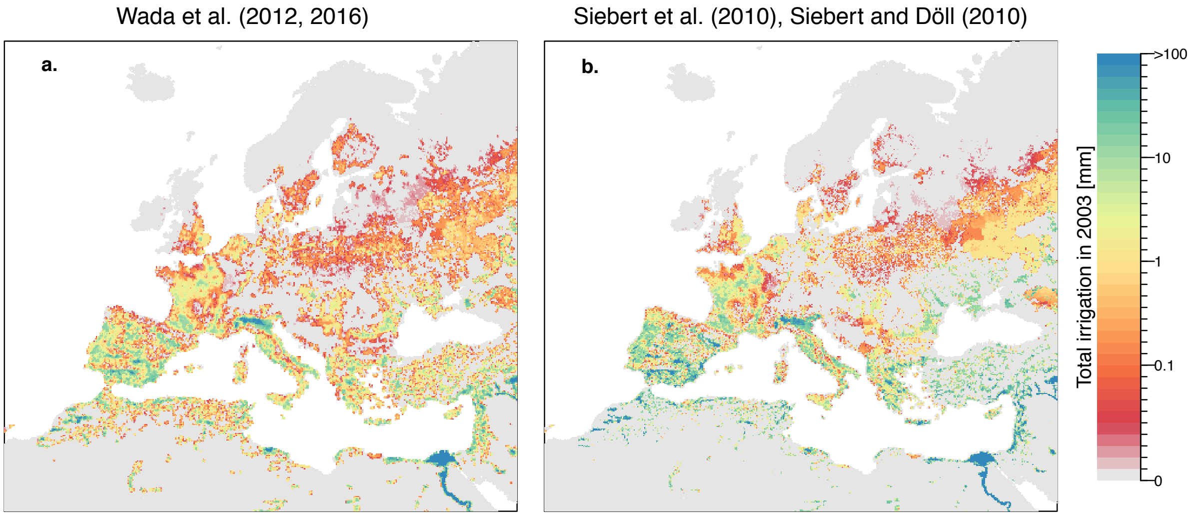
Wada et al. (2012, 2016)

Siebert et al. (2010), Siebert and Döll (2010)

Figure S3. Total irrigation [mm] from both data sets, (a) HWU1, Wada et al. (2012,2016) and (b) HWU2, Siebert et al. (2010), Siebert and Döll (2010), bilinearly interpolated to the European CORDEX domain at 0.11° resolution.

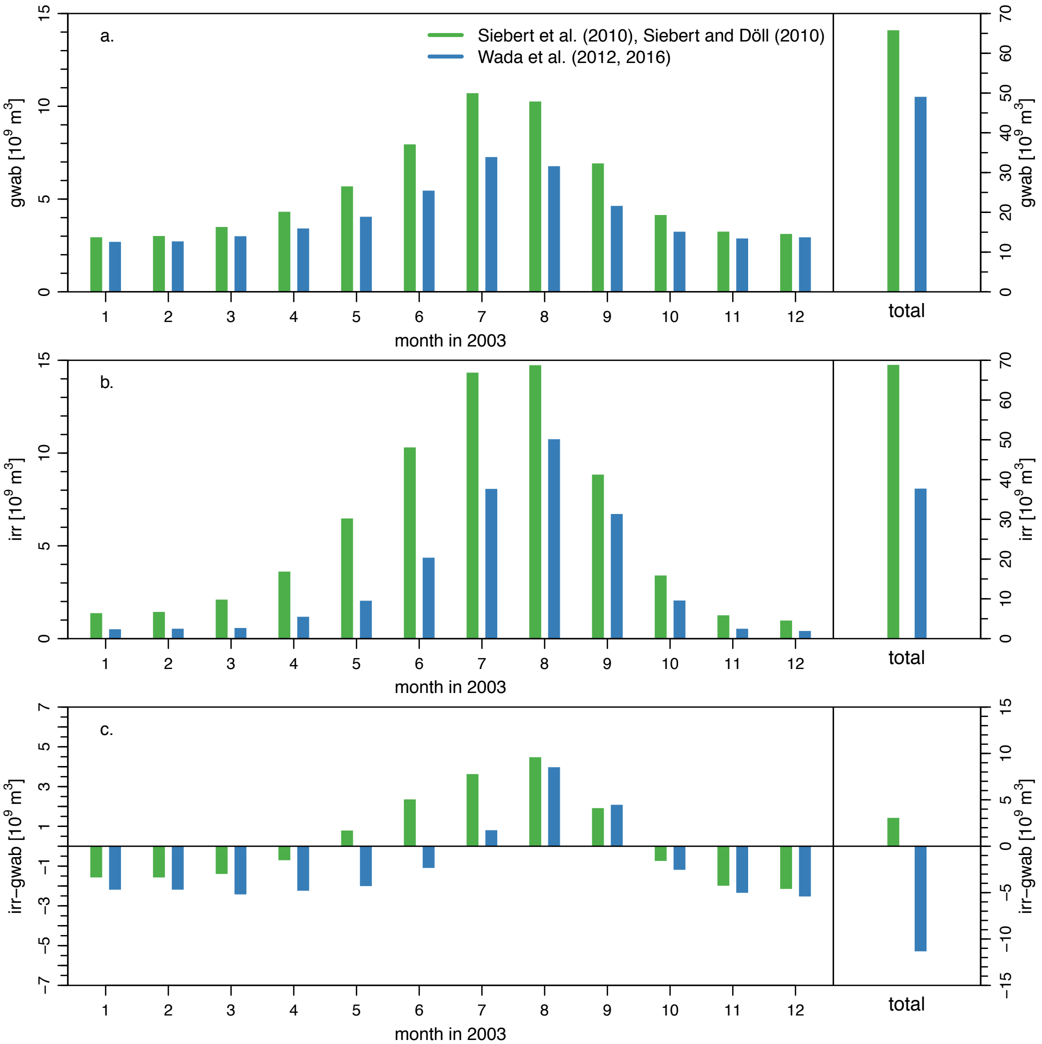

Figure S4. Monthly sums of (a) groundwater abstraction [m^3], (b) irrigation (m^3) and (c) their differences as (irrigation-groundwater abstraction) for both data sets (blue: HWU1, i.e. Wada et al. (2012,2016), green: HWU2, i.e. Siebert et al. (2010), Siebert and Döll (2010)) over the European CORDEX domain for the year 2003.

5 Results – supporting figures and tables

Table S1. Atmospheric divergence (div(Q)) simulated with the natural reference run (NAT) and the 4 water use scenarios (HWU1-1, HWU1-2, HWU2-1, HWU2-2) over the entire year 2003, averaged over the land surface of the entire CORDEX domain. The last column indicates whether the difference between HWU and NAT is significant at the 95% confidence interval (CI; * = significantly different) using all grid points in a paired t-test (df=50303).

	div(Q) **[mm]**	$\Delta(\mathrm{div}(Q))_{\mathrm{HWU-NAT}}$ **[mm]** (95% CI)	$\Delta(\mathrm{div}(Q))_{\mathrm{HWU-NAT}}$ **[%]**	Significant difference (t-value, p-value)
NAT	-459,88	--	--	--
HWU1-1	-459,09	+0,78 (0.24 – 1.33)	-0,17	* (t=2,83; p< 0.05)
HWU1-2	-456,64	+3,23 (2.70 – 3.76)	-0,70	* (t=11,91; p<0.001)
HWU2-1	-458,27	+1,60 (1.07 – 2.14)	-0,35	* (t=5,91; p<0.001)
HWU2-2	-457,80	+2,08 (1.55 – 2.61)	-0,45	* (t=7.67; p<0.001)

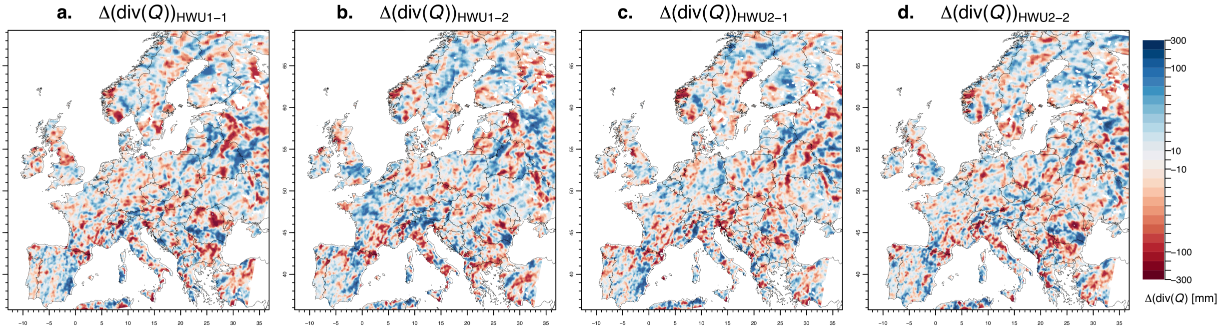

Figure S5. $\Delta(\mathrm{div}(Q))_{\mathrm{HWU-NAT}}$ [mm] over the full CORDEX domain for all water use scenarios (a. HWU1-1, b. HWU1-2, c. HWU2-1, d. HWU2-2) over the full year 2003.

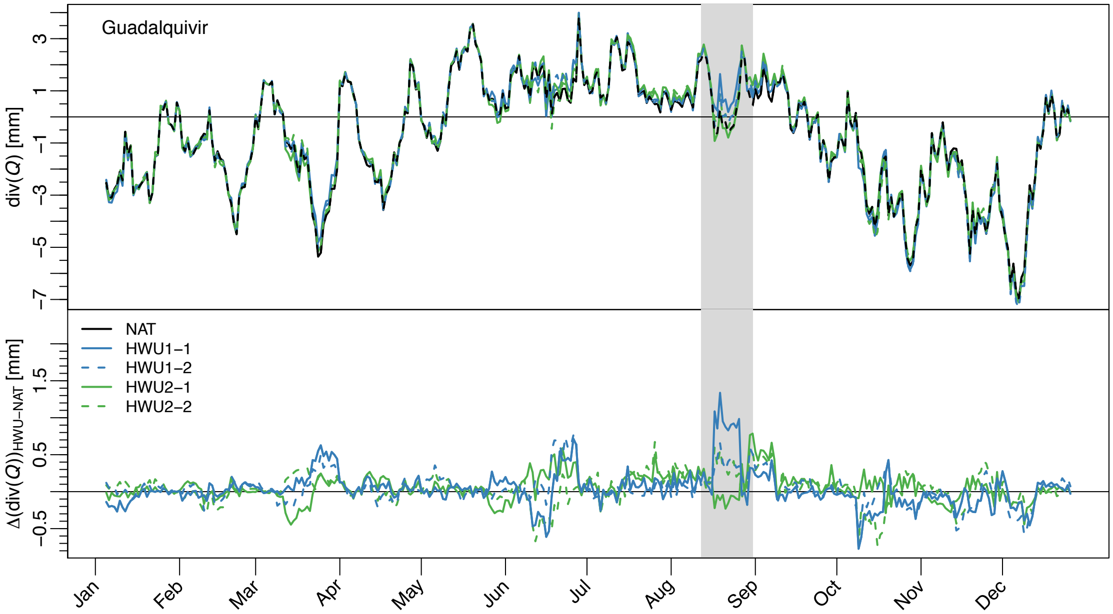

Figure S6. Time series of div(*Q*) [mm] and Δ(div(*Q*)) [mm] averaged over the Guadalquivir basin (Iberian Peninsula). A 10-day-running mean was used for better illustration. Negative values of div(*Q*) illustrate that the land is a sink of moisture, and positive values illustrate that the land provides moisture to the atmosphere. Note that human water use can potentially reverse this balance as illustrated in August by HWU1-1.

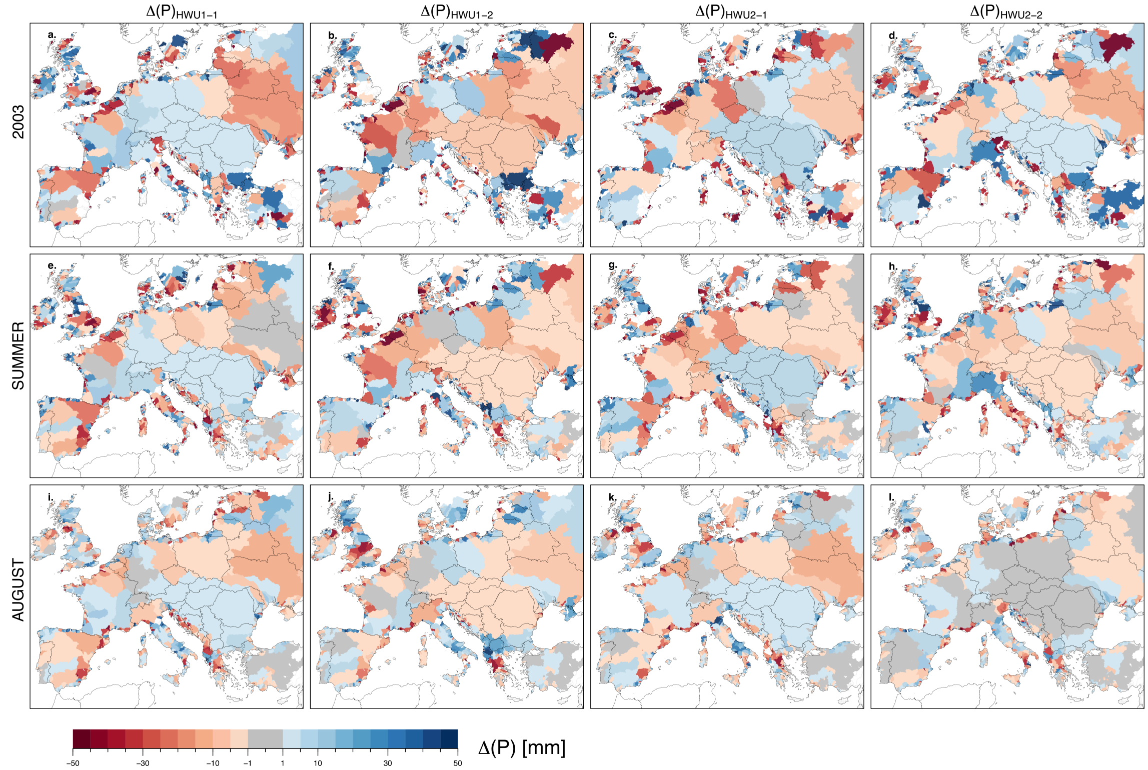

Figure S7. Human water use-induced amplification or attenuation of precipitation (ΔP) [mm] over European watersheds for all water use scenarios along the columns (HWU1-1 (a,e,i), HWU1-2 (b,f,j), HWU2-1 (c,g,k), HWU2-2 (d,h,l)) over the full year 2003 (a-d), summer 2003 (JJA, e-h), and August 2003 (i-l). Watersheds with P differences between -1mm and 1mm are marked grey.

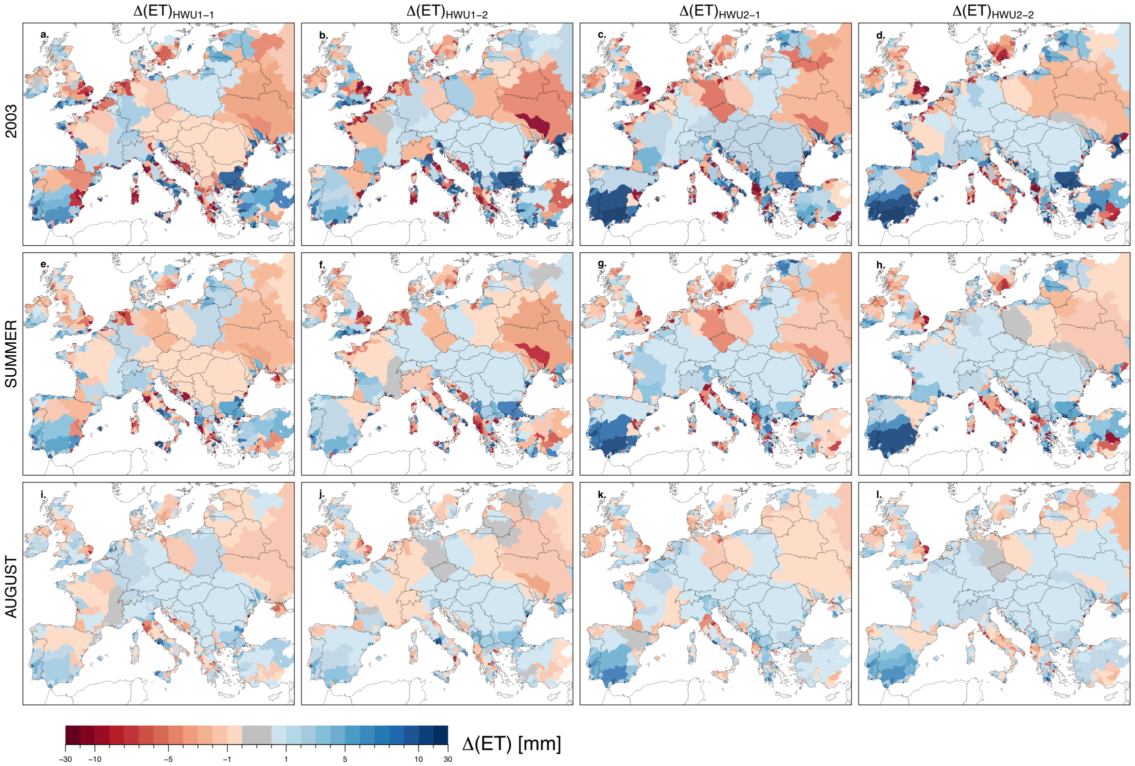

Figure S8. Simulated human water use-induced amplification or attenuation of evapotranspiration (ΔET [mm] as HWU-NAT) over European watersheds for all water use scenarios along the columns (HWU1-1 (a,e,i), HWU1-2 (b,f,j), HWU2-1 (c,g,k), HWU2-2 (d,h,l)) over the full year 2003 (a-d), summer 2003 (JJA, e-h), and August 2003 (i-l). Watersheds with ET differences between -0.1mm and 0.1mm are marked grey.

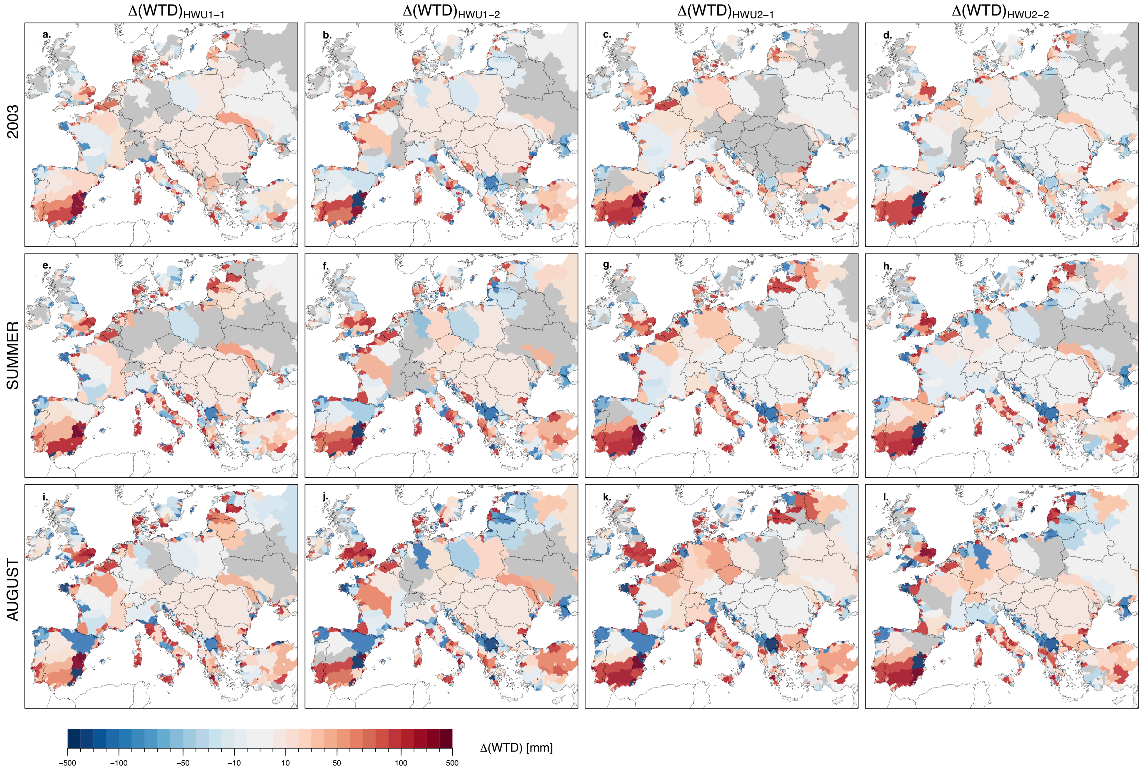

Figure S9. Simulated human water use-induced groundwater table rise (blue) or decline (red) (Δ*WTD* [mm]) over European watersheds for all water use scenarios along the columns (HWU1-1 (a,e,i), HWU1-2 (b,f,j), HWU2-1 (c,g,k), HWU2-2 (d,h,l)) over the full year 2003 (a-d), summer 2003 (JJA, e-h), and August 2003 (i-l). *WTD* differences between -5mm and 5mm are masked grey.

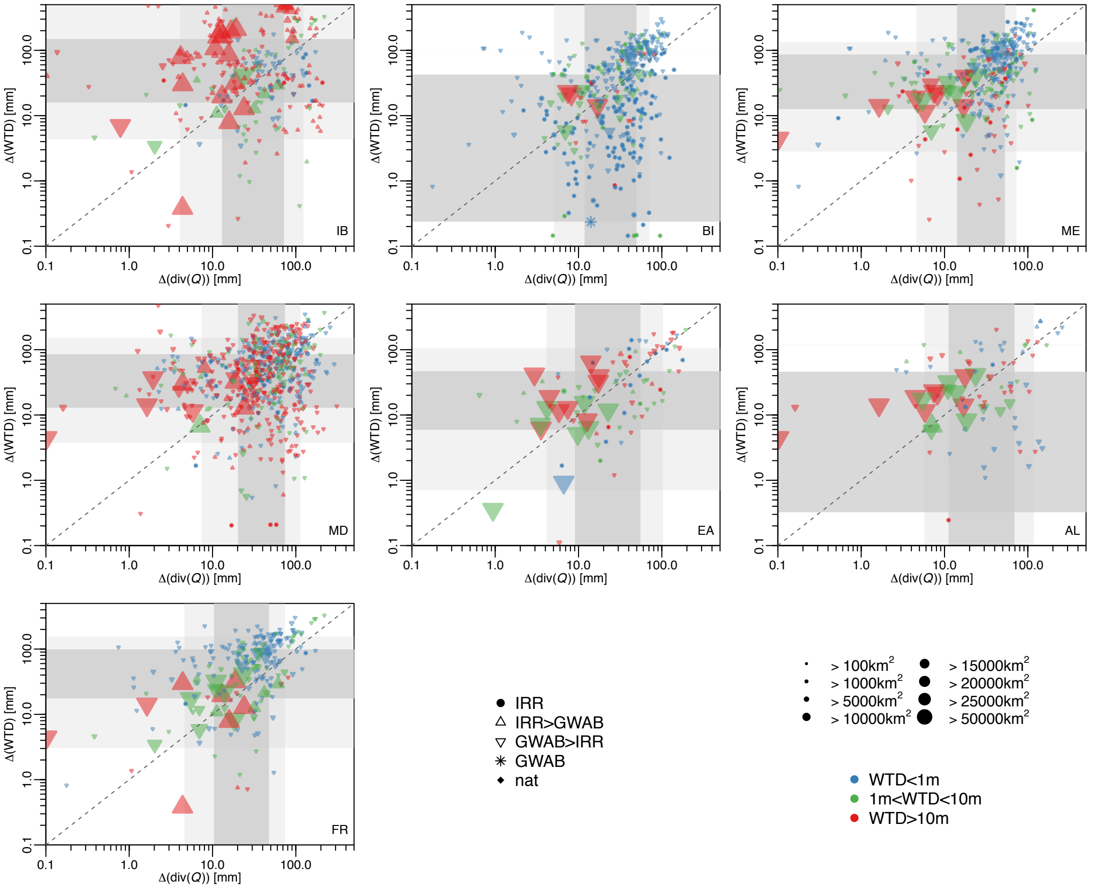

Figure S10. Water table declines Δ*WTD* as a function of changes of the atmospheric sink Δ(div(*Q*)) [mm] for all watersheds in the PRUDENCE regions IP (Iberian Peninsula), BI (British Isles), ME (Mid-Europe), MD (Mediterranean), EA (Eastern Europe), AL (Alps) and FR (France). The colors represent the reference water table depth (blue: shallow (0-1m), green: medium (1-5m), red: deep (>5m)). The size of the symbols is commensurate with the watershed size. The symbols illustrate the most dominant water use. All water use scenarios considered.

6 Validation of the simulations with in-situ observations

We validated daily precipitation and daily evapotranspiration from all simulations (NAT, HWU1-1, HWU1-2, HWU2-1, HWU2-2) with rain gauge observations from the European Climate Assessment & Data (ECA&D, http://www.ecad.eu) data set, and with eddy covariance measurements from FLUXNET (Baldocchi et al., 2001, http://fluxnet.fluxdata.org). The half-hourly values of FLUXNET are accumulated to daily latent heat fluxes and converted to daily evapotranspiration (excluding missing values consistently from model results). For the validation with rain gauge observations, simulations are interpolated to the stations using the nearest neighbor method. A total of 1246 stations are used for validation, with 27 stations over the PRUDENCE region France, 83 over the Iberian Peninsula, 77 over Eastern Europe, 28 over the Mediterranean, 78 over the Alps and 953 over Mid-Europe. For the comparison with FLUXNET stations, the nearest neighbor is used irrespective of the prevalent land cover. This allows us to assess the accuracy of evapotranspiration at 28 towers across Europe with varying land cover types i.e. evergreen broadleaf forest (EBF, 4 towers); deciduous broadleaf forest (DBF, 7 towers); evergreen needleleaf forest (ENF, 6 towers); mixed forest (MF, 1 tower); grassland (GRA, 9 towers) and crop (CRO, 1 station).

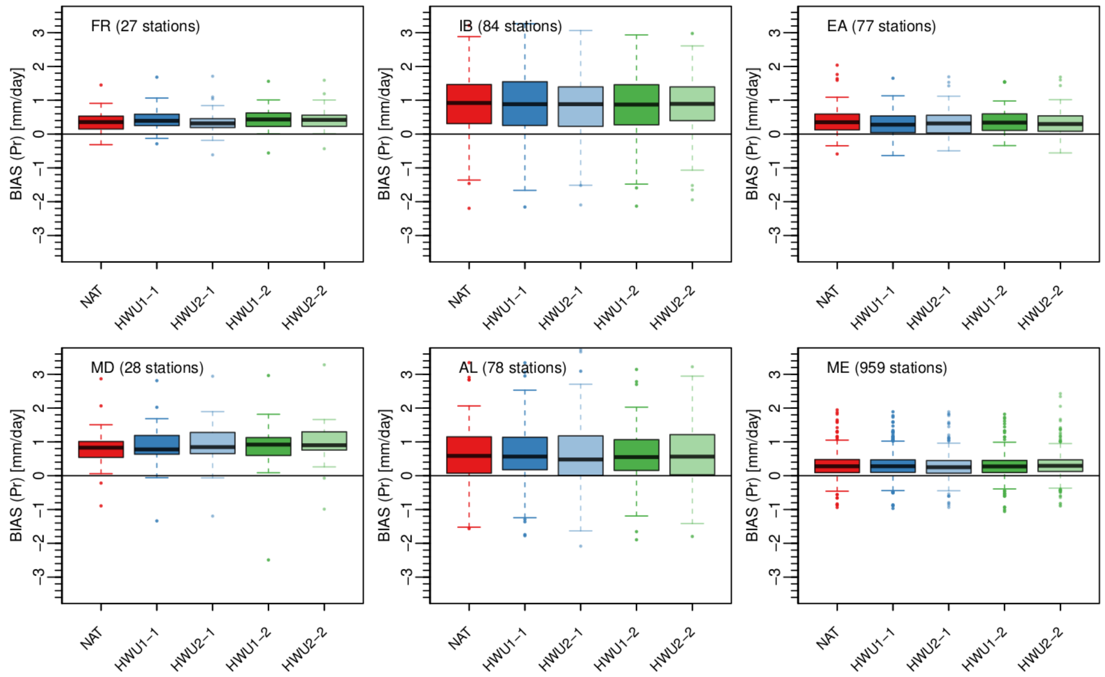

Figure S11. Box-whisker plots of the daily precipitation bias (simulations - observation) in mm/day for all stations within the respective PRUDENCE regions, evaluated with ECA&D stations over the entire year 2003. The number in the top of each subplot shows the total number of stations available for that period.

Figure S10, as shown above, shows the annual precipitation bias (mm/day) for all ECA&D rain gauge observations over the PRUDENCE regions France (FR), Iberian Peninsula (IP), Eastern Europe (EA), Mediterranean (MD), Alps (AL) and Mid-Europe (ME). The figure shows that all simulations exhibit a wet bias from 0.2 to 1 mm/day. Especially southern Europe (the

Mediterranean and the Iberian Peninsula), as well as the Alps show a wet bias on the order of 1mm/day. This agrees well with common regional climate model validations (e.g., Kotlarksi et al., 2017; Katragkou et al., 2015). However, precipitation in Mid- and Eastern Europe, as well as France is more accurate and shows only a small, but wet bias. Vice versa, summer precipitation can be underestimated, as shown in Fig. S11. Summer precipitation is underestimated for all simulations over the Iberian Peninsula and the Mediterranean (-1 mm/day) and has only a small wet bias for the rest of Europe. The difference in the mean biases between all simulations is comparably small and does not allow for any skill assessment.

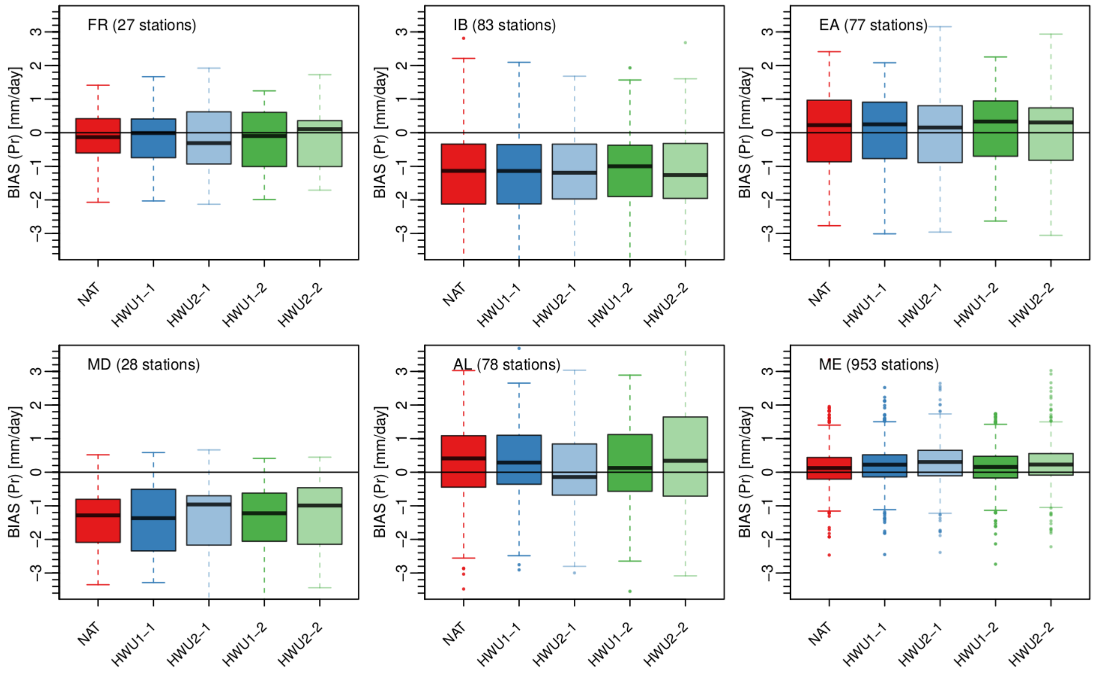

Figure S12. Box-whisker plots of the daily summer precipitation bias (simulations - observation) in mm/day for all stations within the respective PRUDENCE regions, evaluated with ECA&D stations over June-July-August 2003. The number in the top of each subplot shows the total number of stations available for that period.

This tendency for overestimated precipitation may in turn lead to an overestimation of evapotranspiration. The location of all FLUXNET towers used for validation is shown in Fig. S12 and Fig. S13 shows the annual and summer evapotranspiration biases at these stations. However, there is no clear tendency visible at the available towers. Nevertheless, some stations, such as FR-Puc, IT-Cpz, IT-on, IT-SRo and PT-Mi1 are clearly overestimating evapotranspiration. Interestingly, these are mainly southern (IT, PT) or heat wave affected locations (FR), which might indicate that the simulations are not water-limited enough (potentially arising from the wet precipitation bias). A similar conclusion can be drawn from the summer evaporation bias. Nevertheless, there are also a few stations which underestimate evapotranspiration and/or have only a comparably small bias (< ±1mm/day). However, there is no clear pattern with respect to the land use type visible. Considering also the observational uncertainty, the large areal representativeness of the simulated evapotranspiration in contrast to the small footprint of the tower, and the fact that we did not filter for the land use type, indicates that the simulations agree reasonably well with the observations with a tendency for overestimating evapotranspiration. This has also been shown in previous studies and strongly depends on the spatial resolution of the coupled modeling system (Shrestha et al., 2015). Again, all simulations perform similarly, but there are some differences for e.g. summer evapotranspiration at IT-Non, HU-Bug and IT-Ro1 and IT-Ro2 visible, which indicate an impact of human water management.

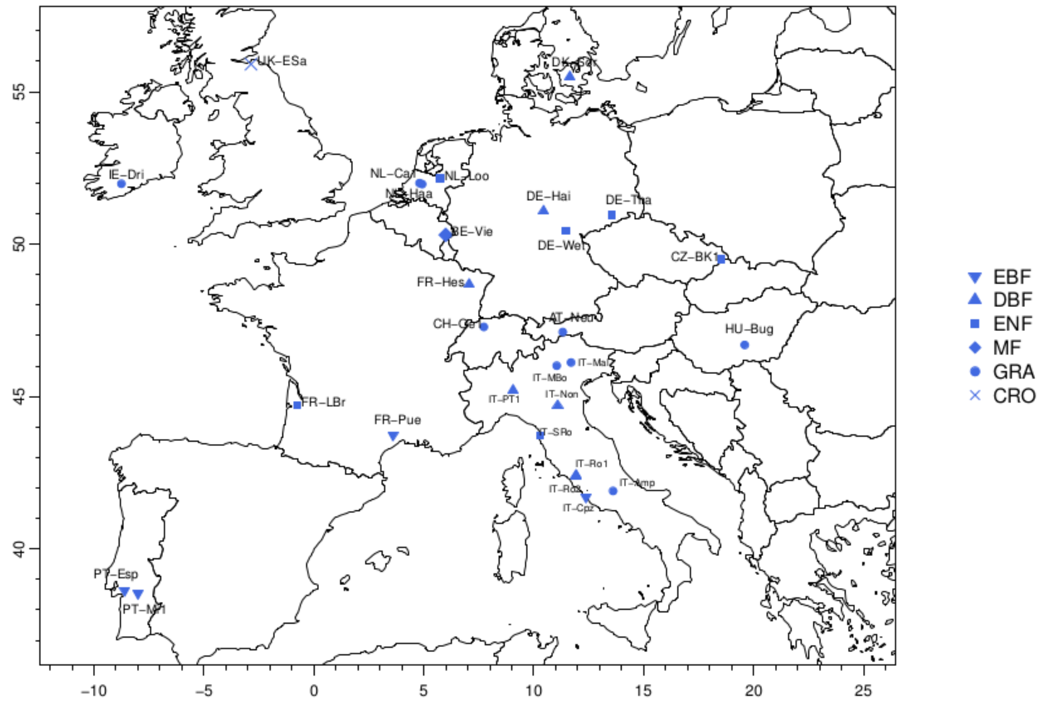

Figure S13. Locations of FLUXNET towers available in 2003. The symbols indicate the dominant land cover.

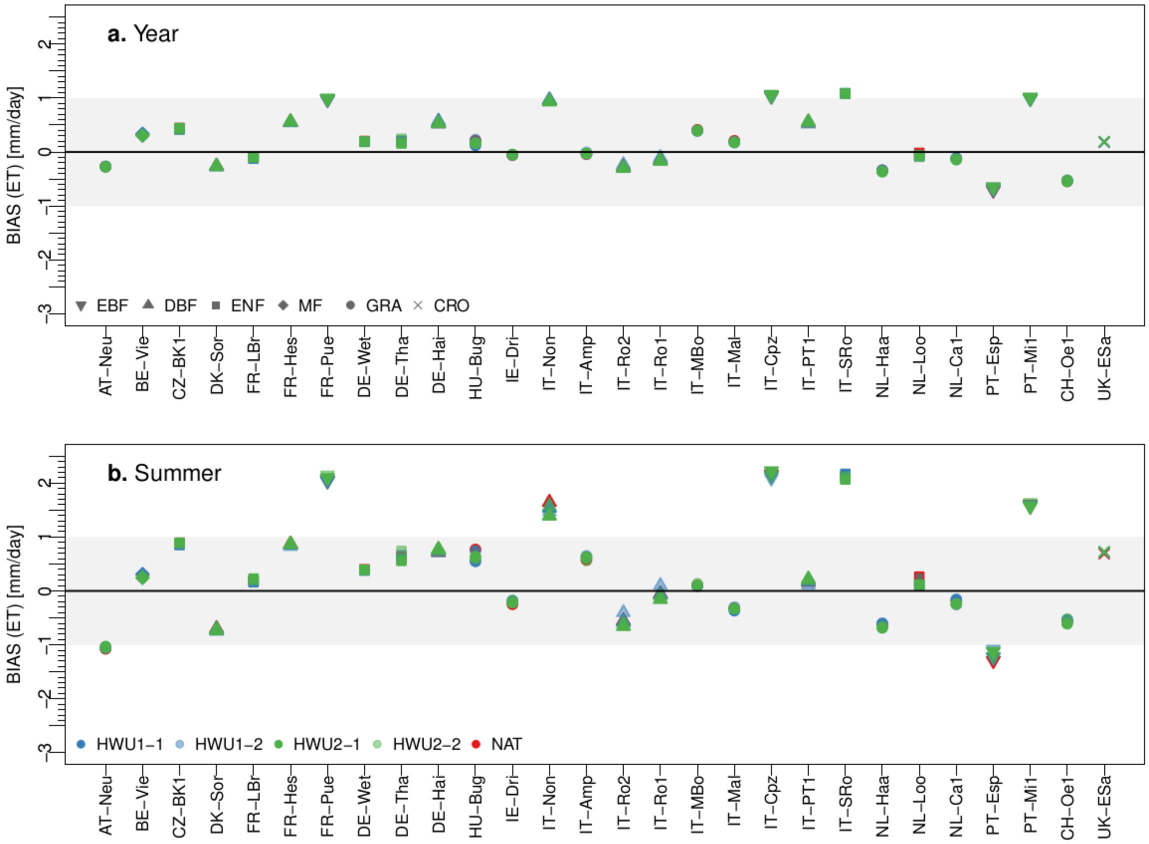

Figure S14. Daily evapotranspiration bias (simulations - observation) in mm/day for all available FLUXNET stations for (a) the entire year 2003 and (b) June-July-August 2003. Colors represent the simulation scenario and symbols indicate the dominant land use type of the FLUXNET tower.

References

Baldauf, M. Seifert, A., Förstner, J., Majewski, D., Raschendorfer, M., & Reinhardt, T. (2011). Operational convective-scale numerical weather prediction with the COSMO model: description and sensitivities. *Monthly Weather Review*, 139(12), 3887-3905. https://doi.org/10.1175/MWR-D-10-05013.1

Baldocchi, D., Falge, E., Gu, L., Olson, R., Hollinger, D., Running, S., ... & Fuentes, J. (2001). FLUXNET: A new tool to study the temporal and spatial variability of ecosystem–scale carbon dioxide, water vapor, and energy flux densities. *Bulletin of the American Meteorological Society*, 82(11), 2415-2434.

Christensen, J. H., & Christensen, O. B. (2007). A summary of the PRUDENCE model projections of changes in European climate by the end of this century. *Climatic change*, 81, 7-30. https://doi.org/10.1038/421805a

Dee, D. P., Uppala, S. M., Simmons, A. J., Berrisford, P., Poli, P., Kobayashi, S., ... Vitart, F. (2011). The ERA‐Interim reanalysis: Configuration and performance of the data assimilation system. *Quarterly Journal of the Royal Meteorological Society*, 137(656), 553-597. https://doi.org/10.1002/qj.828

Doms, G., & Schättler, U. (2002). A description of the nonhydrostatic regional model LM. Deutscher Wetterdienst.

Friedl, M. A., McIver, D. K., Hodges, J. C. F., Zhang, X. Y., Muchoney, D., Strahler, A. H., … Schaaf, C. (2002). Global land cover mapping from MODIS: algorithms and early results. *Remote Sensing of Environment*, 83(1), 287-302. https://doi.org/10.1016/S0034-4257(02)00078-0

Gasper, F., Goergen, K., Shrestha, P., Sulis, M., Rihani, J., Geimer, M., & Kollet, S. (2014). Implementation and scaling of the fully coupled Terrestrial Systems Modeling Platform (TerrSysMP v1. 0) in a massively parallel supercomputing environment–a case study on JUQUEEN (IBM Blue Gene/Q). *Geoscientific model development*, 7(5), 2531-2543. https://doi.org/10.5194/gmd-7-2531-2014

Gleeson, T., Smith, L., Moosdorf, N., Hartmann, J., Dürr, H. H., Manning, A. H., van Beek, L. P. H., & Jellinek, A. M. (2011). Mapping permeability over the surface of the Earth. *Geophysical Research Letters*, 38, L02401. http://doi.wiley.com/10.1029/2010GL045565

Jones, J. E., & Woodward, C. S. (2001), Newton–Krylov-multigrid solvers for large-scale, highly heterogeneous, variably saturated flow problems. *Advances in Water Resources*, 24(7), 763-774. https://doi.org/10.1016/S0309-1708(00)00075-0

Katragkou, E., García-Díez, M., Vautard, R., Sobolowski, S., Zanis, P., Alexandri, G., ... & Goergen, K. (2015). Regional climate hindcast simulations within EURO-CORDEX: evaluation of a WRF multi-physics ensemble. *Geoscientific model development*, 8(3), 603.

Keune, J., Gasper, F., Goergen, K., Hense, A., Shrestha, P., Sulis, M., & Kollet, S. (2016). Studying the influence of groundwater representations on land surface‐atmosphere feedbacks during the European heat wave in 2003. *Journal of Geophysical Research: Atmospheres*, 121(22). https://doi.org/10.1002/2016JD025426.

Kollet, S. J., & Maxwell, R. M. (2006). Integrated surface–groundwater flow modeling: A free-surface overland flow boundary condition in a parallel groundwater flow model. *Advances in Water Resources*, 29(7), 945-958. https://doi.org/10.1016/j.advwatres.2005.08.006

Kotlarski, S., Keuler, K., Christensen, O. B., Colette, A., Déqué, M., Gobiet, A., Goergen, K., Jacob, D., Lüthi, D., van Meijgaard, E., Nikulin, G., Schär, C., Teichmann, C., Vautard, R., Warrach-Sagi, K., and Wulfmeyer, V. (2014). Regional climate modeling on European scales: a joint standard evaluation of the EURO-CORDEX RCM ensemble, Geoscientific Model Development, 7, 1297-1333.

Lehner, B., Verdin, K., & Jarvis, A. (2006). HydroSHEDS technical documentation, version 1.0. *World Wildlife Fund US*, Washington, DC, 1-27.

Lobell, D., Bala, G., Mirin, A., Phillips, T., Maxwell, R., & Rotman, D. (2009). Regional differences in the influence of irrigation on climate. *Journal of Climate*, 22(8), 2248-2255. https://doi.org/10.1175/2008JCLI2703.1

Oleson, K. W., Niu, G.-Y., Yang, Z.-L., Lawrence, D. M., Thornton, P. E., Lawrence, P. J., … Qian, T. (2008). Improvements to the Community Land Model and their impact on the hydrological cycle. *Journal of Geophysical Research: Biogeosciences*, 113(G1). https://doi.org/10.1029/2007JG000563

Ritter, B., & Geleyn, J.-F. (1992). A comprehensive radiation scheme for numerical weather prediction models with potential applications in climate simulations. *Monthly Weather Review*, 120 (2), 303–325.

Shrestha, P., Sulis, M., Masbou, M., Kollet, S., & Simmer, C. (2014). A scale-consistent terrestrial systems modeling platform based on COSMO, CLM, and ParFlow. *Monthly Weather Review*, 142(9), 3466-3483. https://doi.org/10.1175/MWR-D-14-00029.1

Siebert, S. & Döll, P. (2010). Quantifying blue and green virtual water contents in global crop production as well as potential production losses without irrigation. *Journal of Hydrology*, 384(3-4),198-217. https://doi.org/10.1016/j.jhydrol.2009.07.031

Siebert, S., Burke, J., Faures, J. M., Frenken, K., Hoogeveen, J., Döll, P., & Portmann, F. T. (2010). Groundwater use for irrigation – a global inventory. *Hydrology and Earth System Sciences*, 14, 1863-1880. https://doi.org/10.5194/hess-14-1863-2010

Tiedtke, M. (1989). A comprehensive mass flux scheme for cumulus parameterization in large-scale models. *Monthly Weather Review*, 117(8), 1779-1800. https://doi.org/10.1175/1520-0493(1989)117<1779:ACMFSF>2.0.CO;2

Valcke, S. (2013). The OASIS3 coupler: A European climate modelling community software. *Geoscientific Model Development*, 6(2), 373–388. https://doi.org/10.5194/gmd-6-373-2013

Vautard, R., Gobiet, A., Jacob, D., Belda, M., Colette, A., Déqué, M., … Yiou, P. (2013). The simulation of European heat waves from an ensemble of regional climate models within the EURO-CORDEX project. Climate Dynamics, 41(9–10), 2555–2575.

von Storch, H., Langenberg, H., & Feser, F. (2000). A spectral nudging technique for dynamical downscaling purposes. *Monthly Weather Review*, 128(10), 3664-3673. https://doi.org/10.1175/1520-0493(2000)128<3664:ASNTFD>2.0.CO;2

Wada, Y., Beek, L., & Bierkens, M. F. P. (2012). Nonsustainable groundwater sustaining irrigation: A global assessment. *Water Resources Research*, 48(6). https://doi.org/10.1029/2011WR010562

Wada, Y., de Graaf, I. E. M., & van Beek, L. P. H. (2016). High-resolution modeling of human and climate impacts on global water resources. *Journal of Advances in Modeling Earth Systems*, 8, 735–763. https://doi.org/ 10.1002/2015MS000618